Atomic-scale investigation of implanted Mg in GaN through ultra-high-pressure annealing

Jun Uzuhashi[1*], Jun Chen[1*], Ashutosh Kumar[1, a)], Wei Yi[1, b)], Tadakatsu Ohkubo[1], Ryo Tanaka[2], Shinya Takashima[2], Masaharu Edo[2], Kacper Sierakowski[3], Michal Bockowski[3, 4], Hideki Sakurai[4, 5, c)], Tetsu Kachi[4], Takashi Sekiguchi[1,6], and Kazuhiro Hono[1]

[1]*National Institute for Materials Science, Tsukuba, 305-0047, Japan*

[2]*Advanced Technology Laboratory, Fuji Electric Co., Ltd., Hino, Tokyo 191-8502, Japan*

[3]*Institute of High Pressure Physics Polish Academy of Sciences, Sokolowska 29/37, 01-142 Warsaw, Poland*

[4]*IMass, Nagoya University, Aichi 464-8603, Japan*

[5]*AIT, ULVAC, Inc., Chigasaki, Kanagawa 253-8543, Japan*

[6]*University of Tsukuba, Tsukuba 305-8577, Japan*

[*] Authors to whom correspondence should be addressed:

UZUHASHI.Jun@nims.go.jp and CHEN.Jun@nims.go.jp

[a)] *Present address: RISE Research Institutes of Sweden, Lund 223 70, Lund, Sweden*

[b)]*Present address: Kyoto University, Kyoto 615-8510, Japan*

[c)]*Present address: ADDC, Toshiba Electronic Devices & Storage Corporation, Ishikawa 923-1293, Japan*

Abstract

An area selective doping via ion implantation is a key technology to realize gallium nitride (GaN) based energy-efficient power devices; however, conventional annealing leads to the formation of numerous Mg-enriched defects, which result in inefficient *p*-type activation. Recent invention of ultra-high-pressure annealing (UHPA) has enabled a significant improvement of *p*-type activation efficiency. In this study, we investigated the formation of Mg-enriched defects in Mg implanted GaN followed by annealing under either conventional atmospheric pressure or ultra-high-pressure. Unlike the conventional annealing, UHPA leads to much lower number density of Mg-enriched defects. Correlative scanning transmission electron microscopy (STEM), atom probe tomography (APT), cathodoluminescence (CL) and secondary ion mass spectrometry (SIMS) analyses have shown that the number density of Mg-enriched defects are substantially suppressed by the UHPA. The dissolved Mg concentrations in the GaN matrix for both the conventional and the UHPA samples are almost of the same value, approximately 2×10^{18} cm^{-3}; however, the UHPA sample shows over one order of magnitude stronger intensity of donor-acceptor-pair (DAP) emission than the conventional one. Thus, the implanted Mg is effectively activated as acceptors through the UHPA technique.

Introduction

Gallium nitride (GaN) is a promising candidate for the next generation energy-efficient devices in high-power applications [1-3]. An ion implantation technique is a key technology to precisely control area selective conduction types for designing devices. *n*-type conduction is relatively easy by Si ion implantation; however, an inefficient activation of implanted Mg for *p*-type GaN is a critical issue that must be overcome to realize GaN-based high-power devices [4, 5]. Mg ion implantation on GaN inevitably introduces defects, resulting in low activation efficiency compared with Mg doping via epitaxial growth [6-9]. Although a post-implantation annealing at around 1573 K is commonly carried out for the recovery of these defects and for migrating implanted Mg ions into Ga sites as acceptors, an efficient *p*-type activation has not been achieved yet by conventional annealing under N_2 at an atmospheric pressure [6-8]. The inefficient activation was due to the formation of vacancy-type defects and Mg-enriched defects [9, 10]. Based on positron annihilation study, Uedono *et al.* reported that vacancy-type defects were introduced by ion implantation and these vacancies started agglomerating above 1273 K, leading to the formation of vacancy clusters [9]. The vacancy clusters interacted with implanted Mg during the post-implantation annealing and thus resulted in the formation of undesired Mg-enriched defects [10]. Atom probe tomography (APT) investigation has found that these Mg-enriched defects strongly suppressed donor-acceptor-pair (DAP) emissions linked to Mg activation [11]. Therefore, the optimization of annealing conditions is still under investigation to suppress the formation of Mg-enriched defects.

Recently, an ultra-high-pressure annealing (UHPA) under 1 GPa N_2 was reported to improve the Mg activation efficiency substantially [12-14]. These studies showed that the UHPA sample has over one order of magnitude higher intensities in both DAP and near-band edge (NBE) emissions. So far, the temperature of post-implantation annealing had been limited at around

1573 K because of a serious pyrolysis reaction; on the contrary, UHPA can be carried out at the annealing temperature higher than 1573 K without serious decomposition even without a capping layer [12]. TEM analyses have shown that the conventionally annealed samples have unique oblong-shaped dislocation-loops and considerable amount of small dot-shaped defects [10, 11]. On the other hand, although ring-shaped dislocation-loops are dominantly formed by the UHPA with longer annealing duration at 1573 K or higher temperature annealing such as above 1673 K, *p*-type activation efficiency is significantly improved in these samples [14-16]. Mg ion distribution in the ring-shaped dislocation-loops has not been investigated yet due to the detection limit of STEM energy dispersive X-ray spectroscopy (EDS) technique. It is strongly desired to understand the formation mechanism of these defects in both conventional annealing and UHPA. In this work, we have investigated the atomic-scale three-dimensional distribution of implanted Mg ions by using APT, which is the only method to visualize the distribution of atoms three-dimensionally with nearly atomic spatial resolution (a few Å to sub-nm) and high chemical sensitivity [17]. The chemical sensitivity of APT varies by the materials for analysis and the measuring condition; however, the detection limit of Mg in GaN is confirmed as from higher range of 10^{17} to 1×10^{18} cm^{-3} by our previous APT study [11]. In addition, we carried out STEM analyses for observing dislocation-loops and crystal-lattice defects, and cathodoluminescence (CL) measurements to understand Mg activation as a function of depth. Based on the correlative analyses results, we clarified the underlying mechanism for the significant improvement of *p*-type activation efficiency in the UHPA sample.

Experimental methods

A thick 4 μm homoepitaxial *n*-GaN layer was grown by metal organic chemical vapor

deposition (MOCVD) on [0001] oriented free standing GaN substrate prepared by the standard hydride vapor phase epitaxy (HVPE) technique. The detail of growth is described in previous reports [9-11]. Then, Mg ion implantation was carried out on the *n*-GaN epitaxial layer at room temperature with 20-430 keV to form 500 nm deep box profile with a Mg concentration of 1×10^{19} cm^{-3}. Thereafter, a post-implantation annealing was performed under a N_2 atmosphere for 5 min. Conventional annealing was carried out with an AlN protective capping, whereas UHPA was carried out with no protective capping. The samples were annealed under 0.1 MPa, atmospheric pressure, at 1573 K with a heating rate of 8 K/s for conventional annealing, and under 1 GPa at 1673 K with a heating rate of approximately 0.45 K/s for UHPA. Hereafter, we refer to the sample with conventional annealing at 1573 K as "conventional sample", and the UHPA sample at 1673 K as "UHPA sample". Mg and H concentration profiles as a function of depth were analyzed by using secondary ion mass spectrometry (SIMS). STEM observations were carried out by using a FEI Titan G2 80-200 at 200 kV. APT analyses were carried out to obtain three-dimensional Mg and H ions distributions by using a CAMECA LEAP 5000XS. Both STEM and APT specimens were prepared by the standard lift-out method using a focused ion beam (FIB) with a scanning electron microscopy (SEM) system, FEI Helios G4UX [18, 19]. APT specimens were prepared from approximately 150 nm to 500 nm depth of the sample surface. APT measurements were carried out with 355 nm wavelength laser pulsing at a repetition rate of 250 kHz at a specimen temperature of 30 K. The laser pulse energy was set as 10 fJ to achieve a stoichiometric ratio of 1:1 for Ga:N. The obtained APT data was analyzed by CAMECA Integrated Visualization and Analysis Software (IVAS) 3.8.8. In addition to STEM and APT techniques, CL measurements were made to understand the relationship between the microstructure and the activation efficiency [11]. Angle cutting cross-sectional sample preparation method was carried out to reveal the depth distribution of DAP and NBE emissions

[20]. The CL measurements were carried out by a HORIBA MP32 CL system attached to a Hitachi SU6600 field emission scanning electron microscope (FESEM) at an incident beam energy of 3 kV and a specimen temperature of 78 K. Cross-sectional specimens for CL measurement were prepared by a cross-section polisher (JEOL SM-09010). Chen *et al.* reported the detailed method, and a low energy Ar ion milling enables to prepare the angle cutting cross-sectional sample with less surface damages [20].

Results and Discussions

Figure 1 shows the Mg and H concentration profiles measured by SIMS, in which 500 nm deep box profile is highlighted by a pale green rectangle. Mg concentration in the as-implanted state is drawn by gray dotted line for reference. The Mg concentration in the Mg implanted box is ~1 × 10^{19} cm^{-3} for the conventional sample, which is almost the same as that of the as-implanted sample. The H concentration profile for the conventional sample is below the detection limit (lower range of 10^{16} cm^{-3}). On the other hand, a significant Mg diffusion is observed in the depth direction in the UHPA sample. This enhanced Mg diffusion in the depth direction is reported as one of the features through the UHPA by Sakurai *et al.* [12] and Sierakowski *et al.* [13], and it is considered that the significant Mg diffusion may be assisted by defects induced by ion implantation. The H concentration profile in the UHPA sample is distinctly different from that of the conventional sample. For the UHPA sample, the H concentration is kept as almost the same as the Mg concentration in the depth direction. This enhanced Mg diffusion into the depth direction and a simultaneous Mg-H diffusion by UHPA were reported and discussed by Narita *et al.* and Sakurai *et al.*, and H atoms are considered to be introduced into the sample from the UHPA ambient [21, 22]. As the result of the enhanced Mg diffusion into the depth direction, the Mg concentration in the ion implanted box decreased

to 3~4 × 10^{18} cm^{-3} for the UHPA sample.

Figure 2 shows the low-angle annular dark field (LAADF)-STEM images of (a) the conventional sample and (b) the UHPA sample. LAADF-STEM images are sensitive to distortions of crystal-lattice, whereas high-angle annular dark-field (HAADF)-STEM images are highly sensitive to atomic number Z [23]. Distortion caused by the vacancy-type defects or the Mg clustering gives bright contrast in the LAADF-STEM image. Oblong-shaped defects and numerous small dot-shaped defects are observed in the conventional sample, whereas ring-shaped defects and a few dot-shaped defects are observed in the UHPA sample. Iwata *et al.* reported that the oblong-shaped defects are inversion domain with Mg segregation, and the ring-shaped defects are the extended intrinsic defects by TEM observation [15]. As for the small dot-shaped defect shown in Fig. 2(c), Kumar *et al.* reported these brightly dot-shaped contrasts is attributed to the strain contrast caused by Mg clustering on the *c*-plane by complementary STEM and APT analysis [10]. In addition to these defects, a pyramidal defect is observed at the side of each oblong-shaped defect in the conventional sample as shown in Fig. 2(d), and a bright dot is observed on each ring-shaped defect in the UHPA sample as shown in Fig. 2(e) and (f).

Figure 3(a) and (b) show the numbers of observed defects in Fig. 2(a) and (b) as a function of depth. Firstly, the STEM specimens' thickness was evaluated because the number density of defects can not be compared without the evaluation of STEM specimens' thickness. After that, numbers of defects were counted and compared between two samples. The thickness of STEM specimens can be calculated from zero-loss peak intensity and low-loss intensity obtained by electron energy-loss spectroscopy (EELS) spectrum, and the average mean free path (λ) for GaN. The λ value for GaN was determined to be 0.12 μm by Kumar *et al.* [11]. Here, the thicknesses for both the conventional and the UHPA samples are calculated to be around 20 nm and confirmed well uniform in the depth direction. Fig. 3(a) plots the number of the dot-shaped

defects in the conventional and UHPA samples as function of the depth from the surface of the samples. The number of defects is almost constant within 50 to 550 nm depth for the conventional sample. The number of the oblong-shaped defects is also constant within 50 to 550 nm depth for the conventional sample as shown in Fig. 3(b). On the contrary, the number of small dot-shaped defects is not constant for the UHPA sample, that is, it increases from 250 to 550 nm depth and then gradually decreases in the depth direction. It is hard to conclude the tendency of ring-shaped defects due to very few numbers. Here, Fig. 2 and 3 indicate the following two features: (1) the number density of the defects is much lower in the UHPA sample; (2) these defects are even more suppressed near the sample surface for the UHPA sample, approximately up to 250 nm depth. These features in the UHPA sample are in good agreement with the previous report based on positron annihilation study by Uedono *et al.*; that is, the density of vacancies decreased through UHPA because the sample surface without any protection capping could be an effective sink for vacancies [24]. Thus, the total number of defects has been suppressed and there are few defects near the sample surface in the UHPA sample. The underlying formation mechanism of these unique defects (*i.e.*, oblong-shaped defect, small dot-shaped defect, ring-shaped defect, and dot on each ring-shaped defect) is still under investigations; therefore, this paper focuses on revealing the atomic-scale distribution of implanted Mg as below.

Figure 4 shows the typical three-dimensional Mg ion maps for the conventional and the UHPA samples. The iso-concentration surfaces are drawn for 0.5 at% Mg for the conventional sample and 0.3 at% Mg for the UHPA sample for better visualization of Mg clusters and segregations. The total Mg concentration obtained by APT measurement is 0.013 at% (1.1×10^{19} cm^{-3}) for the conventional sample and 0.004 at% (3.5×10^{18} cm^{-3}) for the UHPA sample; these values are well matched with the SIMS results. The peak of Mg at 12 Da in APT mass

spectra overlaps with carbon; however, carbon concentration is confirmed as about 3×10^{15} cm^{-3} by SIMS measurement. Therefore, Mg distribution and its concentration obtained by APT are well accurate. An extracted Mg ion map for one of the Mg clusters is shown in Fig. 4(b) and the Mg cluster is disk-shaped on the *c*-plane with 1.0~2.0 at%. This result is good agreement with Kumar *et al.*'s investigation; that is, the crystal lattice is expanded along the *c*-axes at the small dot-shaped defects caused by planar-shaped Mg clustering [10]. For the UHPA sample, the Mg segregation on ring-shaped defects is confirmed by APT as shown in Fig. 4(c) and (d). By analyzing all the obtained APT data, the number density of small Mg clusters is calculated as follows. The number density of the Mg clusters in the conventional sample is 2.9×10^{22} m^{-3}; however, it is reduced to 1.4×10^{21} m^{-3} for the UHPA sample, the value is 20 times lower than that in the conventional sample. Note that "Mg cluster" was defined as Mg concentration of over 0.5 at% here and total volume of APT data is about 3.7×10^{7} nm^3 for the conventional sample and 2.0×10^{7} nm^3 for the UHPA sample. Furthermore, the average volume size of the Mg clusters in the UHPA sample is 5.7 nm^3, which is much smaller than that of the conventional sample, 26.7 nm^3. In brief, both the number density and the volume size of Mg clusters are substantially suppressed by UHPA.

Figure 5 shows the three-dimensional Mg ion maps and Mg and H concentration line profiles of the oblong-shaped defect in the conventional sample and the ring-shaped defect in the UHPA sample. All the line profiles were calculated from cylinders with 5 nm in diameter. Mg-enriched pyramidal defect was found at the side of the oblong-shaped defect in the conventional sample as shown in Fig. 5(a). Mg concentrations in the oblong-shaped defect and the top (0001) facet of the pyramidal defect are close to 10 at%. Not only the oblong-shaped defects, but also a lot of Mg clusters with Mg concentration of 1.0~2.0 at% exist in the conventional sample as shown in Fig. 4(a). These highly Mg-enriched defects made the

dissolved Mg concentration in the GaN matrix decreased to 0.0023 at% (2.0×10^{18} cm^{-3}) for the conventional sample. On the other hand, the Mg segregation in the ring-shaped defect in the UHPA sample is much suppressed than that of the oblong-shaped defect. The Mg concentration in the ring-shaped defect is approximately 0.5 at% and in the bright dot 1.0~3.0 at%. Remarkably, H segregation at the pyramidal defect and the bright dot in both samples has been revealed by APT. The background hydrogen is invariably detected from the ultrahigh vacuum chamber for the APT analysis; nevertheless, an obvious increase of H concentration such as 1 to 2 at% is observed in Fig.5 (c) and (f). The background H concentration in GaN matrix is approximately 0.5 at% or below; therefore, 1~2 at% of H is a significant increase. A segregation of H is not observed at the small Mg clusters (data not shown here), and at highly Mg-enriched regions such as the oblong-shaped defect (Fig.5 (b)) and the top facet of the pyramidal defect (Fig.5 (c)). It is known that H is easily bond with Mg substituted at Ga sites [25, 26]. For the bright dot in the UHPA sample, the ratio of Mg:H varies from 1:1 to 2:1 as shown in Fig.5 (f). It suggests the possibility of the formation of Mg-H complexes, and it is supported by a simultaneous Mg-H diffusion observed by SIMS measurement. In the conventional sample, the average H concentration measured by SIMS is below the detection limit (lower range of 10^{16} cm^{-3}) and the source of H atoms is currently unknown; however, the existence of H atoms at the pyramidal defects does not contradict the SIMS result if taking the number density of these defects into account. The profile of Mg is not matched with that of H for the pyramidal defects as shown in Fig.5(c); thus, the finding of local H segregation at the pyramidal defects is mystery at the current stage and required further investigations.

Figure 6 shows the intensities of DAP and NBE emissions as a function of depth for the conventional and UHPA samples. Mg implanted 500 nm deep box is highlighted by pale green rectangle. The intensities of both DAP and NBE emissions of the UHPA sample are one order

of magnitude higher than those of the conventional sample within the implanted box. For the conventional sample, a weak insufficient DAP emission is observed in the Mg implanted box, indicating inefficient activation of implanted Mg. The inefficient recovery of NBE emission in the conventional sample indicates the existence of dense defects, *i.e.,* Mg-enriched defects and vacancy-type defects. For the UHPA sample, the formation of Mg-enriched defects is highly suppressed as confirmed by STEM and APT. Since no remarkable difference in the dissolved Mg concentration in the GaN matrix is observed between the conventional and the UHPA samples, it is indicated that the implanted Mg is effectively migrated to Ga sites by UHPA leading to one order of magnitude stronger DAP emission. The strong DAP emission is observed not only in the Mg implanted 500 nm deep box, but also in a deeper region up to around 1 μm due to an enhanced Mg diffusion. In general, it is considered that Mg atoms are passivated by the formation of acceptor-H neutral pairs [25, 26]. However, strong DAP emission is observed for the UHPA sample in this study. Lyons *et al.* reported that the H can passivate the Mg as acceptors; however, the Mg-H pairs remain optically active [26]. Thus, the DAP emission may be not significantly affected with the presence of H. The recovery of the NBE emission in the UHPA sample is also in good agreement with the lower number density of nonradiative defects, *i.e.,* Mg-enriched defects or vacancy clusters, as confirmed by our STEM and APT analyses, and Uedono *et al.*'s positron annihilation study [24]. Also, Iwata *et al.* suggested that the ring-shaped dislocations in the UHPA may be an effective sink for the vacancies [15].

In the following, how implanted Mg ions and vacancy defects interact with each other during the conventional annealing will be discussed. The magnitude of Mg diffusion is small, therefore Mg concentration in the implanted box has been kept as almost constant ~1×10^{19} cm^{-3}. As Uedono *et al.* reported that the vacancy-type defects are introduced in the as-implanted

state and vacancies are agglomerated during post-implantation annealing [9], then Mg will be segregated at the vacancy clusters and this may lead to the formation of Mg-enriched defects. This mechanism has been confirmed by APT study on Mg clustering [10]. On the other hand, a simultaneous Mg-H diffusion occurs in the UHPA sample and the magnitude of the Mg-H diffusion into the depth direction is significantly enhanced. The underlying mechanism of this enhanced Mg-H diffusion is still unclear because of several factors which should be taken into accounts, including annealing temperature, heating and cooling rates, as well as the role of introduced H atoms and so on. From the viewpoint of average Mg concentration, the value in the implanted box of the UHPA sample decreases to the lower range of 10^{18} cm^{-3}, owing to an enhanced Mg diffusion in the depth direction. Our previous study has revealed that no Mg clustering is observed in the case of Mg concentration of 1×10^{18} cm^{-3} [11]. Here, some possible explanations of how implanted Mg ions, vacancy-type defects and H atoms interact with each other in the UHPA sample are come up; however, further investigations and discussions are required to clarify the detailed mechanism of the UHPA technique.

Based on the correlative analyses by using STEM, APT and CL, the number density of Mg-enriched defects and the dissolved Mg concentration in the GaN matrix could be obtained. For the conventional sample, the formation of large amount Mg-enriched defects made the dissolved Mg concentration in the GaN matrix decreased to 0.0023 at% (2.0×10^{18} cm^{-3}), even though the average Mg concentration obtained by SIMS measurement has been kept as 1×10^{19} cm^{-3}. Considering the dissolved Mg concentration in the GaN matrix ($[Mg_{matrix}]$) and the average Mg concentration measured by SIMS ($[Mg_{average}]$) in 500 nm deep box profile, the ratio of $[Mg_{matrix}]$ to $[Mg_{average}]$ is 20~30 % for the conventional sample, in other words, 70~ 80 % of implanted Mg exist as Mg segregations or small Mg clusters, *i.e.,* nonradiative defects. On the other hand, the number density of Mg-enriched defects in the UHPA sample is 20 times

lower than that in the conventional sample. Not only the number density, but also the Mg segregation at defects in the UHPA sample is substantially suppressed. Although the dissolved Mg concentration in the GaN matrix for the UHPA sample is decreased to 0.0028 at% (2.4×10^{18} cm^{-3}) due to a significant Mg diffusion in the depth direction, the $[Mg_{matrix}]/[Mg_{average}]$ is 70~80 %, which means that the implanted Mg is much more effectively migrated to Ga sites in case of the UHPA. The Mg concentration in the GaN matrix of the UHPA sample is comparable to that of the conventional sample; however, the intensity of DAP emission of the UHPA sample is over one order of magnitude stronger than that of the conventional sample. Hence, the UHPA technique could lead to the effective migration of implanted Mg to Ga sites and the better recovery of defects introduced by ion implantation.

Conclusion

In summary, we have carried out APT, STEM, CL and SIMS correlative analyses of Mg implanted GaN followed by conventional atmospheric pressure annealing and ultra-high pressure annealing (UHPA). The conventional annealing leads to the formation of numerous Mg-enriched defects. On the contrary, the formation of the Mg-enriched defects is grealty suppressed by UHPA. A simultaneous Mg-H diffusion into the depth direction is found in the UHPA sample. APT analyses show that there is no significant difference in the dissolved Mg concentration in the GaN matrix between the conventional and UHPA samples. However, the emission intensities of DAP and NBE from the UHPA sample are one order of magnitude stronger than the conventional sample. It is strongly indicated that the damage caused by ion implantation is well recovered and the implanted Mg is effectively migrated to Ga sites through the UHPA. Thus, the correlative microstructural and CL investigation shown in this paper suggested that the UHPA is promising technique for realizing efficient *p*-type GaN by ion

implantation.

Data availability statement

The data that support the findings of this study are available from the corresponding author upon reasonable request.

Acknowledgements

The support for this research was provided by the Ministry of Education, Culture, Sports, Science and Technology (MEXT), Japan, through its “Program for research and development of next-generation semiconductor to realize energy-saving society” Program Grant No. JPJ005357. Part of this research was also supported by the Polish National Science Centre through Project No. 2018/29/B/ST5/00338 as well as by the Polish National Centre for Research and Development through project TECHMATSTRATEG-III/0003/2019-00. Authors thank Kyoko Suzuki for her technical support.

References

1. I. C. Kizilyalli, A. P. Edwards, O. Aktas, T. Prunty, and D. Bour, IEEE Trans. Electron Devices **62**, 414 (2015).
2. T. J. Flack, B. N. Pushpakaran, and S. B. Bayne, J. Electron. Mater. **45**, 2673 (2016).
3. H. Amano, Y. Baines, E. Beam, M. Borga, T. Bouchet, P. R. Chalker, M. Charles, K. J. Chen, N. Chowdhury, R. Chu, C. De Santi, M. M. De Souza, S. Decoutere, L. Di Cioccio, B. Eckardt, T. Egawa, P. Fay, J. J. Freedsman, L. Guido, O. Häberlen, G. Haynes, T. Heckel, D. Hemakumara, P. Houston, J. Hu, M. Hua, Q. Huang, A. Huang, S. Jiang, H. Kawai, D. Kinzer, M. Kuball, A. Kumar, K. B. Lee, X. Li, D. Marcon, M. März, R. McCarthy, G. Meneghesso, M. Meneghini, E. Morvan, A. Nakajima, E. M. S. Narayanan, S. Oliver, T. Palacios, D. Piedra, M. Plissonnier, R. Reddy, M. Sun, I. Thayne, A. Torres, N. Trivellin, V. Unni, M. J. Uren, M. Van Hove, D. J. Wallis, J. Wang, J. Xie, S. Yagi, S. Yang, C. Youtsey, R. Yu, E. Zanoni, S. Zeltner, and Y. Zhang, J. Phys. D Appl. Phys. **51**, 163001 (2018).
4. Y. Irokawa, O. Fujishima, T. Kachi, and Y. Nakano, J. Appl. Phys. **97**, 083505 (2005).
5. A. J. Fellows, Y. K. Yeo, M. Y. Ryu, and R. L. Hengehold, J. Electron. Mater. **34**, 1157 (2005).
6. T. Narita, T. Kachi, K. Kataoka, and T. Uesugi, Appl. Phys. Express **10**, 016501 (2017).
7. T. Niwa, T. Fujii, and T. Oka, Appl. Phys. Express **10**, 091002 (2017).
8. M. Akazawa, R. Kamoshida, S. Murai, T. Narita, M. Omori, J. Suda, and T. Kachi, Phys. Status Solidi B **257**, 1900367 (2019).
9. A. Uedono, S. Takashima, M. Edo, K. Ueno, H. Matsuyama, W. Egger, T. Koschine, C. Hugenschmidt, M. Dickmann, K. Kojima, S. F. Chichibu, and S. Ishibashi, Phys. Status Solidi B **255**, 1700521 (2018).
10. A. Kumar, J. Uzuhashi, T. Ohkubo, R. Tanaka, S. Takashima, M. Edo, and K. Hono, J. Appl.

Phys. **126**, 235704 (2019).

11. A. Kumar, W. Yi, J. Uzuhashi, T. Ohkubo, J. Chen, T. Sekiguchi, R. Tanaka, S. Takashima, M. Edo, K. Hono, J. Appl. Phys. **128**, 065701 (2020).
12. H. Sakurai, M. Omori, S. Yamada, Y. Furukawa, H. Suzuki, T. Narita, K. Kataoka, M. Horita, M. Bockowski, J. Suda, and T. Kachi, Appl. Phys. Lett. **115**, 142104 (2019).
13. K. Sierakowski, R. Jakiela, B. Lucznik, P. Kwiatkowski, M. Iwinska, M. Turek, H. Sakurai, T. Kachi and M. Bockowski, Electronics **9**, 1380 (2020).
14. T. Nakashima, E. Kano, K. Kataoka, S. Arai, H. Sakurai, T. Narita, K. Sierakowski, M. Bockowski, M. Nagao, J. Suda, Appl. Phys. Express **14** 011005 (2021).
15. K. Iwata, H. Sakurai, S. Arai, T. Nakashima, T. Narita, K. Kataoka, M. Bockowski, M. Nagao, J. Suda, T. Kachi, and N. Ikarashi, J. Appl. Phys. **127**, 105106 (2020).
16. K. Sumida, K. Hirukawa, H. Sakurai, K. Sierakowski, M. Horita, M. Bockowski, T. Kachi and J. Suda, Appl. Phys. Express **14**, 121004 (2021).
17. T.F. Kelly, Rev. Sci. Instrum. **78**, 031101 (2007).
18. M. Schaffer, B. Schaffer, Q. Ramasse, Ultramicroscopy **114**, 62-71 (2012).
19. K. Thompson, D. Lawrence, D.J. Larson, J.D. Olson, T.F. Kelly, B. Gormanb, Ultramicroscopy **107**, 131-139 (2007).
20. J. Chen, W. Yi, T. Kimura, S. Takashima, M. Edo, and T. Sekiguchi, Appl. Phys. Express **12**, 051010 (2019).
21. T. Narita, H. Sakurai, M. Bockowski, K. Kataoka, J. Suda and T. Kachi, Appl. Phys. Express **12,** 111005 (2019).
22. H. Sakurai, T. Narita, M. Omori, S. Yamada, A. Koura, M. Iwinska, K. Kataoka, M. Horita, N. Ikarashi, M. Bockowski, J. Suda and T. Kachi, Appl. Phys. Express **13**, 086501 (2020).
23. P. J. Phillips, M. De Graef, L. Kovarik, A. Agrawal, W. Windl, and M. J. Mills,

Ultramicroscopy **116**, 47–55 (2012).

24. A. Uedono, H. Sakurai, T. Narita, K. Sierakowski, M. Bockowski, J. Suda, S. Ishibashi, S.F. Chichibu & T. Kachi, Sci. Rep. **10**, 17349 (2020).
25. S. Nakamura, N. Iwasa, M. Senoh and T. Mukai, Jpn. J. Appl. Phys. **31**, 1258 (1992).
26. J. L. Lyons, A. Janotti, and C. G. Van de Walle, Phys. Rev. Lett. **108**, 156403 (2012).

Captions

Figure 1. Mg and H concentration profiles measured by SIMS, in which 500 nm deep box profile is highlighted by a rectangle with pale green color. Mg concentration in the as-implanted state is drawn by gray dotted line for reference.

Figure 2. LAADF-STEM images of (a) the conventional sample and (b) the UHPA sample. (c) One of the dot-shaped defects with higher magnification. (d) Magnified STEM image for a part of the oblong-shaped defect indicated by a yellow square in (a). The pyramidal defect is indicated by an arrow and the text in (d). (e) Magnified STEM image for the ring-shaped defect indicated by a yellow square in (b). (f) Magnified STEM image for the dot on the ring-shaped defect indicated by a yellow square in (e).

Figure 3. Numbers of defects as a function of depth. (a) dot-shaped defects; (b) oblong-shaped defects and ring-shaped defects in the LAADF-STEM images of Fig. 2(a) and (b).

Figure 4. Three-dimensional Mg ion maps for (a) the conventional sample and (c) the UHPA sample. The iso-concentration surfaces of Mg are drawn for (a) 0.5at% and (c) 0.3 at% for better visualization of Mg clusters and segregations. An extracted three-dimensional Mg ion map for (b) one Mg cluster and (d) the ring-shaped defect.

Figure 5. Extracted three-dimensional Mg ion maps of (a) oblong-shaped defect in the conventional sample and (d) ring-shaped defect in UHPA sample. Mg and H concentration line profiles through (b) oblong-shaped defect, (c) pyramidal-defect, (e) ring-shaped defect and (f) bright dot indicated by red arrows in (a) and (d).

Figure 6. Intensities of (a) DAP and (b) NBE emission as a function of depth for the conventional sample and the UHPA sample. Mg implanted 500 nm deep box is highlighted by pale green rectangle.

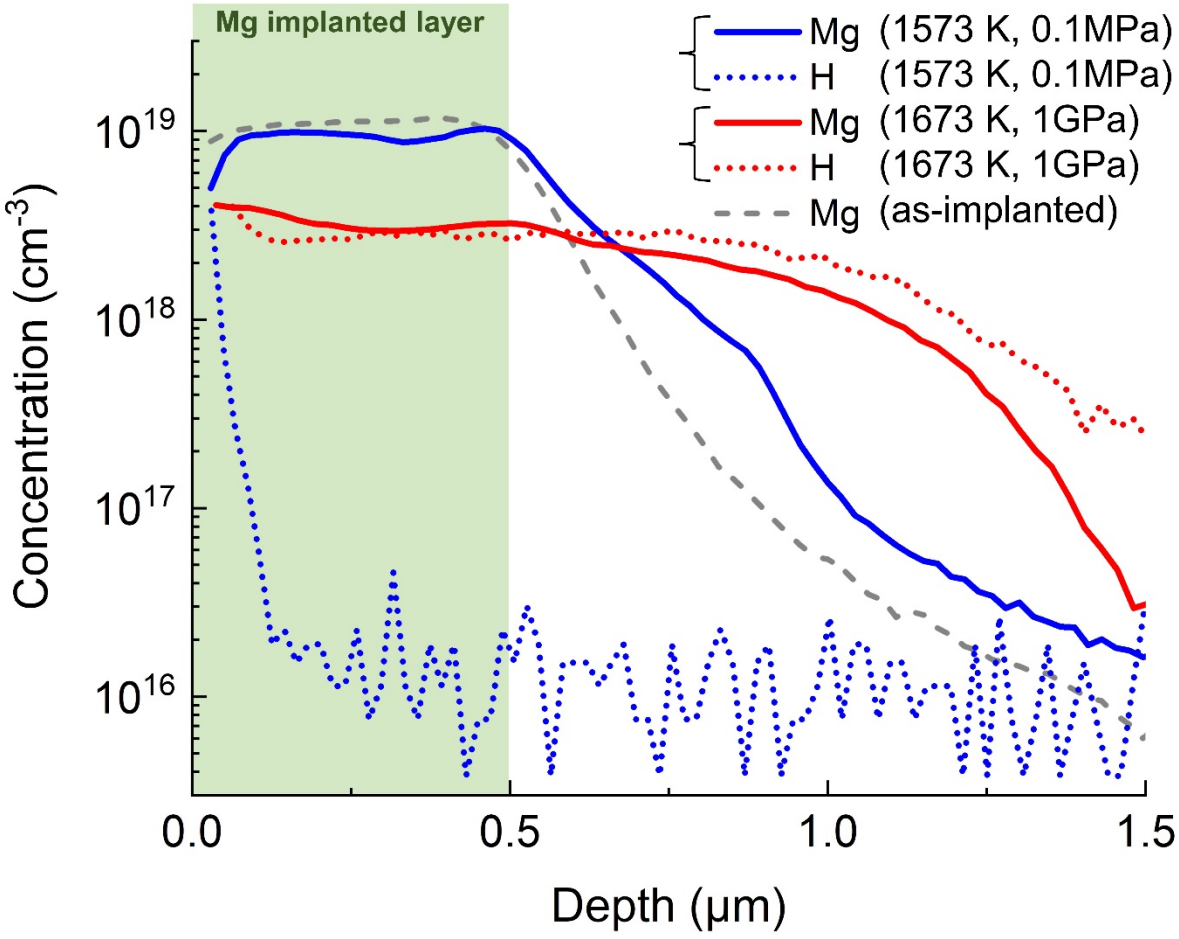

Figure 1. Mg and H concentration profiles measured by SIMS, in which 500 nm deep box profile is highlighted by a rectangle with pale green color. Mg concentration in the as-implanted state is drawn by gray dotted line for reference.

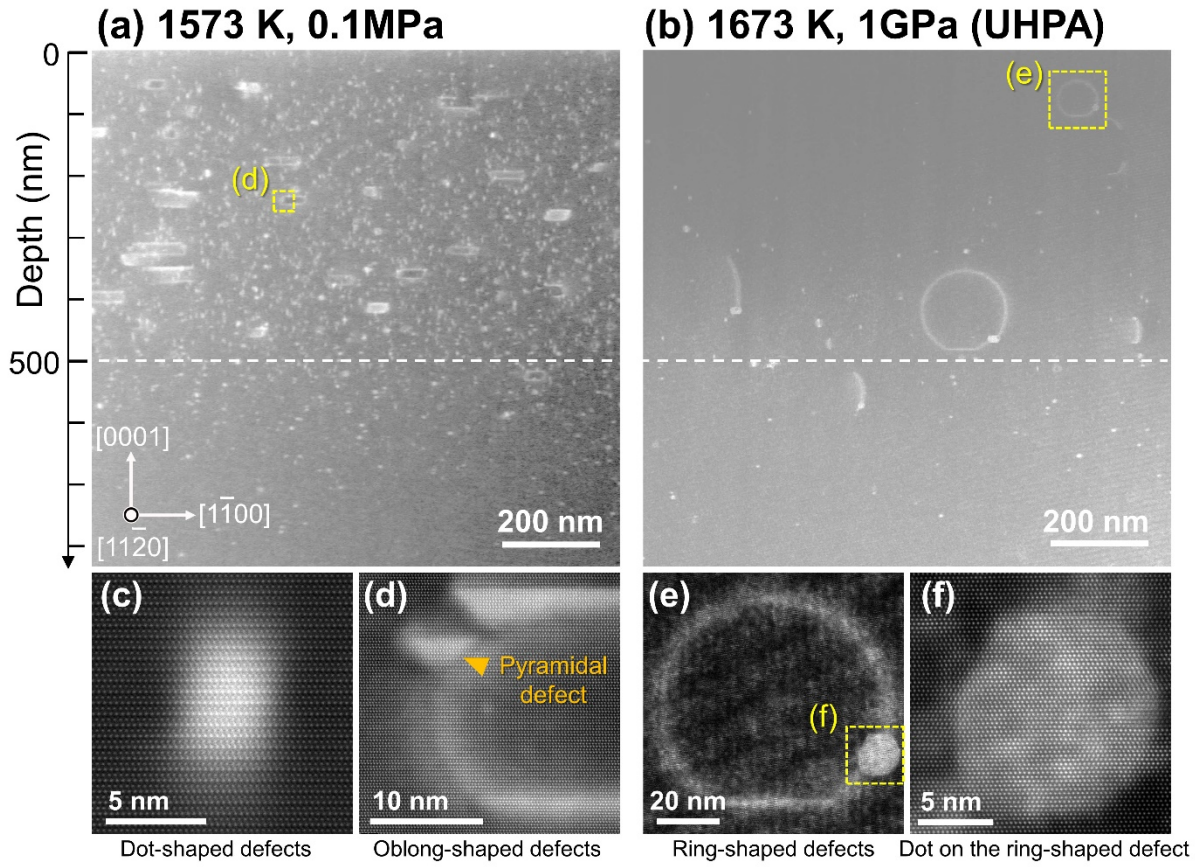

Figure 2. LAADF-STEM images of (a) the conventional sample and (b) the UHPA sample. (c) One of the dot-shaped defects with higher magnification. (d) Magnified STEM image for a part of the oblong-shaped defect indicated by a yellow square in (a). The pyramidal defect is indicated by an arrow and the text in (d). (e) Magnified STEM image for the ring-shaped defect indicated by a yellow square in (b). (f) Magnified STEM image for the dot on the ring-shaped defect indicated by a yellow square in (e).

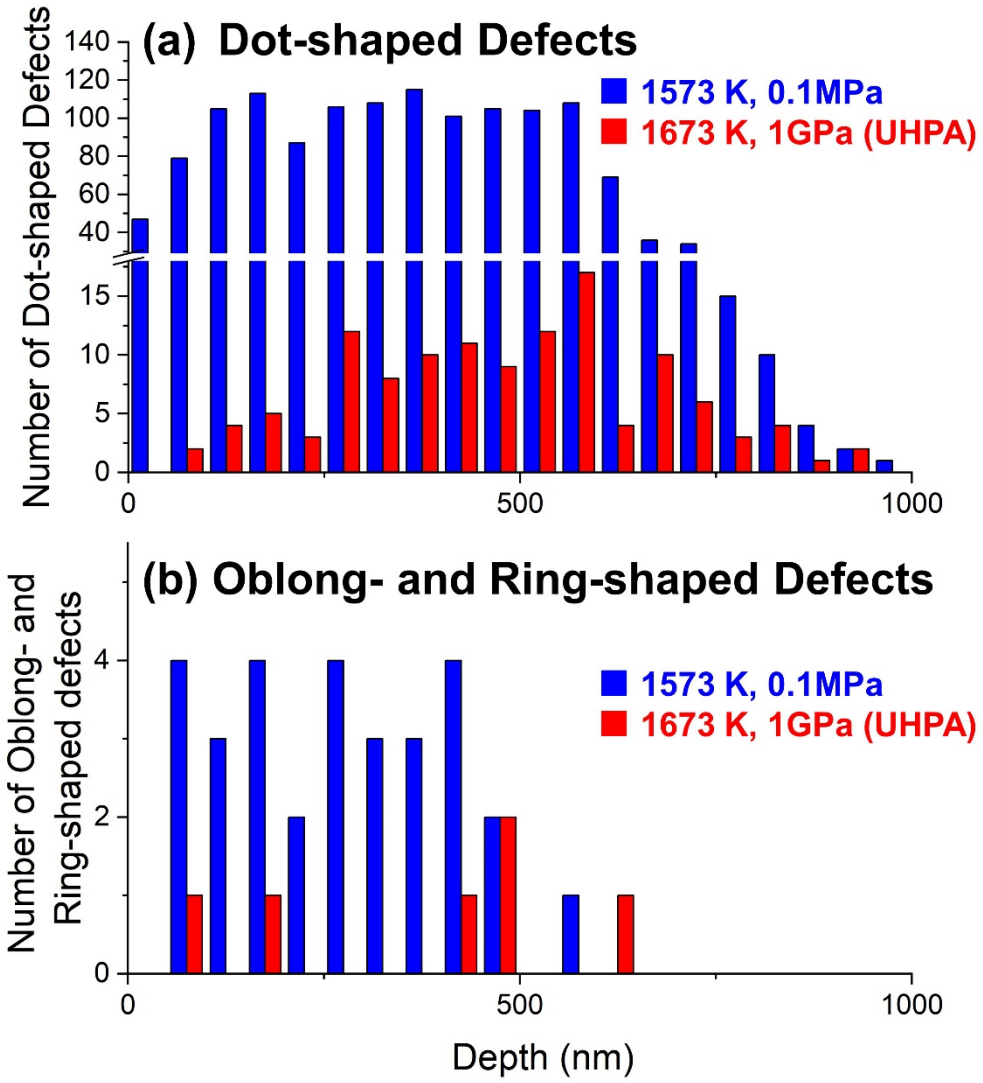

Figure 3. Numbers of defects as a function of depth. (a) dot-shaped defects; (b) oblong-shaped defects and ring-shaped defects in the LAADF-STEM images of Fig. 2(a) and (b).

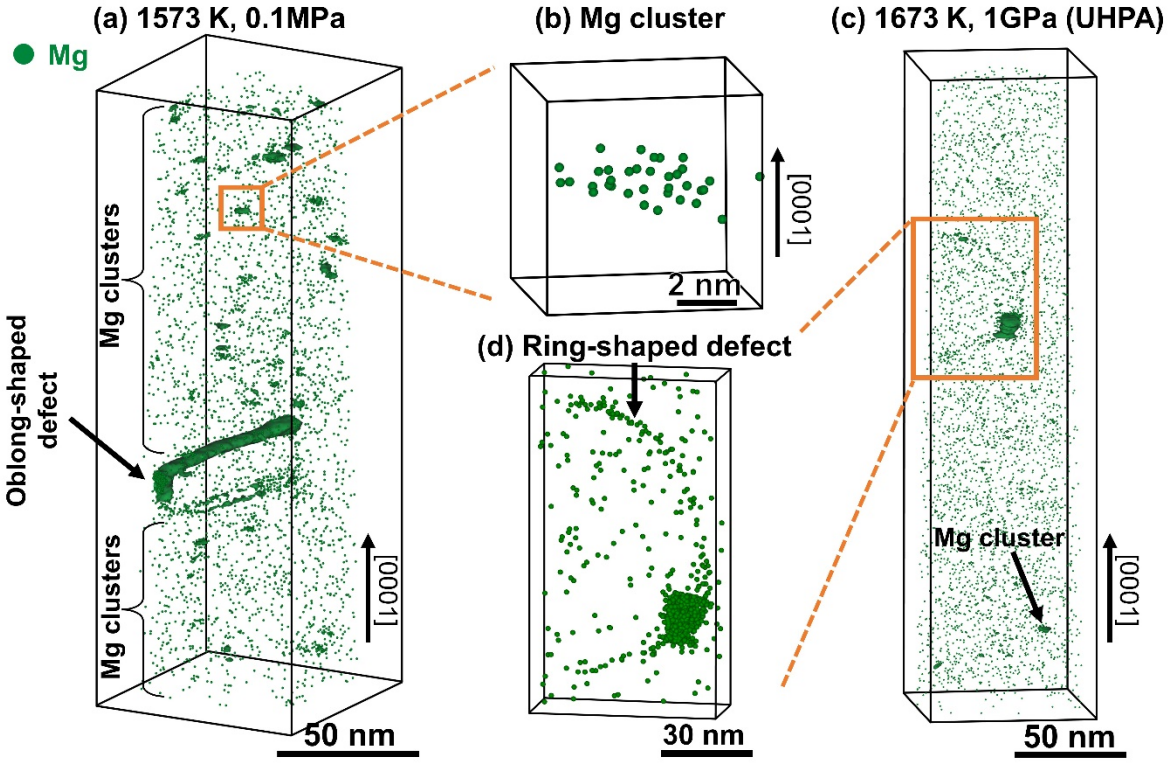

Figure 4. Three-dimensional Mg ion maps for (a) the conventional sample and (c) the UHPA sample. The iso-concentration surfaces of Mg are drawn for (a) 0.5at% and (c) 0.3 at% for better visualization of Mg clusters and segregations. An extracted three-dimensional Mg ion map for (b) one Mg cluster and (d) the ring-shaped defect.

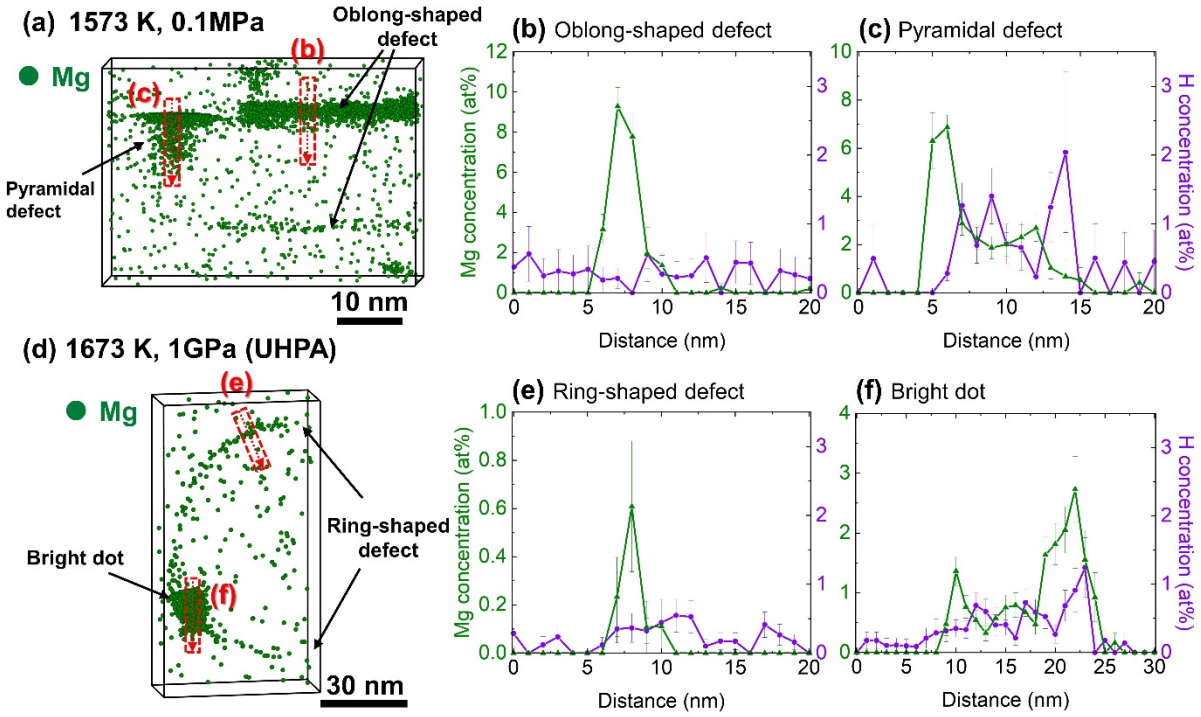

Figure 5. Extracted three-dimensional Mg ion maps of (a) oblong-shaped defect in the conventional sample and (d) ring-shaped defect in UHPA sample. Mg and H concentration line profiles through (b) oblong-shaped defect, (c) pyramidal-defect, (e) ring-shaped defect and (f) bright dot indicated by red arrows in (a) and (d).

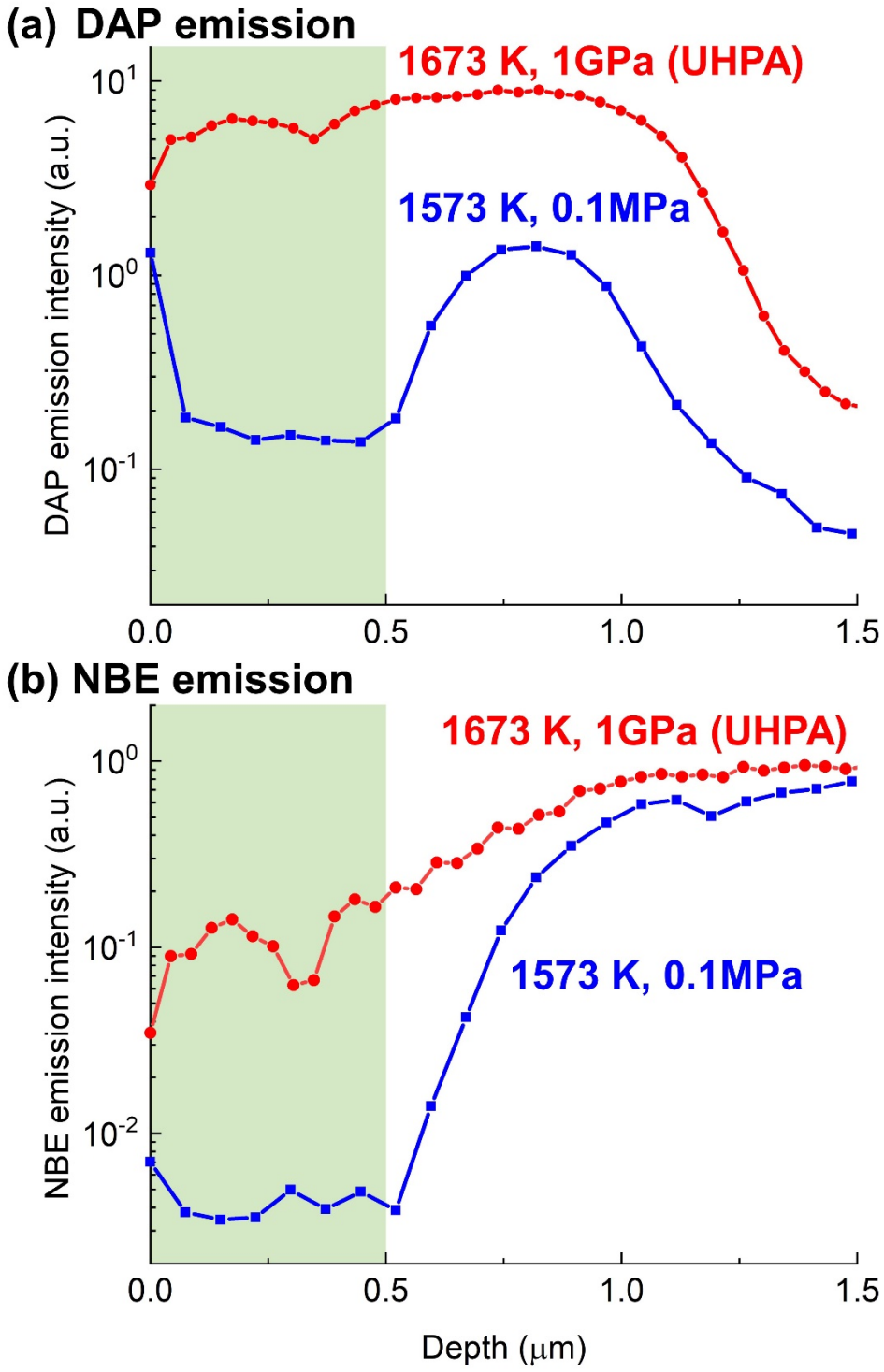

Figure 6. Intensities of (a) DAP and (b) NBE emission as a function of depth for the conventional sample and the UHPA sample. Mg implanted 500 nm deep box is highlighted by pale green rectangle.